Exploring molecular structures, orbital interactions, intramolecular proton-transfer reaction kinetics, electronic transitions and complexation of 3-hydroxycoumarin species using DFT methods

Nuttawisit Yasarawan [a], Khajadpai Thipyapong [a,*], Vithaya Ruangpornvisuti [b]

[a] *Department of Chemistry, Faculty of Science, Burapha University, Chonburi 20131, Thailand*
[b] *Department of Chemistry, Faculty of Science, Chulalongkorn University, Bangkok 10330, Thailand*

ARTICLE INFO

ABSTRACT

Optimal structures and electronic properties of various species of 3-hydroxycoumarin (3-HCou) have been explored using density functional theory (DFT) methods under polarizable continuum model (PCM) of solvation. Electron transfer from pyrone to benzene moieties is enhanced upon deprotonation. Anionic and radical species have similar orbital-interaction characteristics but the charges in the former are distributed more uniformly. The rate of intramolecular proton transfer for the neutral species increases many folds upon excitation. The HOMO–LUMO transition with $\pi \rightarrow \pi^*$ character mainly accounts for the UV absorption of most 3-HCou species in solution. The wavelengths of maximal absorption predicted using TD-DFT method are in agreement with the previous experiment. For the charged species, calculations with the range-corrected functional yield better agreement with the previous experiment. Anionic 3-HCou species shows high degrees of complexation with chromium(III) and copper(II) compared with oxovanadium(IV) and zinc(II). Either oxovanadium(IV) or zinc(II) prefers forming two isomeric complexes with comparable degrees of formation.

© 2014 Elsevier Inc. All rights reserved.

1. Introduction

Hydroxycoumarins form a class of coumarin derivatives which play important roles in the development of pharmacologically active compounds and healthcare products. A number of hydroxycoumarin-based compounds and their metal complexes have anticoagulant, antioxidant, antimicrobial, anti-HIV and antiviral properties [1–5]. Particular synthetic 4-hydroxycoumarin-based compounds such as warfarin and acenocoumarol are known as vitamin K antagonists clinically used in the treatment of blood clotting [1,3]. 7-Hydroxycoumarin (or umbelliferone), a naturally occurring hydroxycoumarin, is used as an active ingredient in sunscreen formulation [6] and its derivatives have been reported as showing significant antioxidant and anti-inflammatory properties [1,7–10]. Several previous researches show that a number of synthetic dyes containing fluorogenic hydroxycoumarin moieties are desirable for use as laser dyes, chemosensors or molecular probes [11–14]. Recently, a pH-sensitive fluorescent dye derived from 7-hydroxycoumarin has been used in the preparation of a novel quencher-free molecular beacon for probing target nucleic acid sequences and the probing mechanism relies on the change of acidity of such the dye upon hybridization of complementary strands of DNA [15]. Previously, appropriate doses of particular transition metal ions such as chromium(III) [16–18], zinc(II) [19–23], copper(II) [24–26] and oxovanadium(IV) [20,21,27,28] have been found to play significant roles in satisfactorily reducing plasma glucose levels both in vitro and in vivo. In several cases, compared to the unbound metal ions, the complexes formed by such the metal ions show superior therapeutic properties as the carbohydrate and lipid metabolic activities are frequently regulated by the biochemically active complexes formed by proteins and metal ions [29–31]. In terms of drug release, gradual collapse of coordination center of complexes would allow optimal release of therapeutic metal ions to bloodstream. Kostova et al. [32,33] previously reported that the complexes prepared from 4-methyl-7-hydroxycoumarin ligand and lanthanide or transition metal ions showed promising pharmacological properties such as spasmolytic, anticoagulant and cytotoxic activities. Nevertheless, finding more appropriate and less harmful ligands in the preparation of drugs is still an active topic in pharmacological research area. 3-Hydroxycoumarin (3-HCou), so far, has not received much attention compared to its isomers. However, in terms of coordination chemistry, a molecule
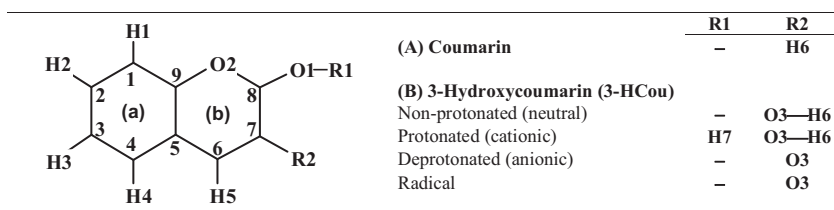
Scheme 1. Skeleton of (A) coumarin and (B) chemical species originating from 3-hydroxycoumarin (3-HCou) with atom-labeling system included. Benzene and pyrone ring moieties are denoted by (a) and (b), respectively.

of 3-HCou depicted in Scheme 1 can be regarded as a potential bidentate ligand using its *ortho* oxygen atoms, i.e. O1 and O3, as donor atoms in the metal-ion chelation. Since a series of hydroxylated 3-HCou compounds have been found to show antioxidant activities comparable to those of quercetin and vitamin C [4]; therefore, theoretical and experimental studies of complexation between pharmacologically active metal ions and 3-HCou may offer the principle of developing novel compounds with multiple therapeutic properties.

In the present study, 3-HCou has been theoretically treated as a model ligand to form complexes with the following transition metal ions: chromium(III), zinc(II), copper(II) and oxovanadium(IV). However, prior to the study of metal–ligand complexation, the details about structural and electronic properties of the ligand itself should be well comprehended. Thus, stable molecular structures for non-protonated, protonated, deprotonated and radical species of 3-HCou have been determined by means of full geometry optimization under the density functional theory (DFT) in association with the polarizable continuum model (PCM). There have been a number of DFT studies on the molecular structures and excited-state properties of 7-hydroxycoumarin and 7-hydroxy-4-methylcoumarin in solution [34,35]. Here, a variety of structural and electronic properties related to the stability and reactivity such as charge density distributions, hydrogen bonding, bond orbital interactions and frontier molecular orbital energies have been well described for the optimal structures of 3-HCou species. The theoretical kinetic study of intramolecular proton-transfer (IPT) reaction of 3-HCou has been attempted, allowing the prediction of activation energies for such the reaction either in the ground state or excited state. Effects of metal–ligand stoichiometry, donor-atom configuration or coordination by water molecules on the stability and absorption properties of the complexes have been theoretically examined. For each type of metal ions, the most favorable scheme of complexation has been established based on the thermodynamic energies of complexation. Theoretically predicted UV–visible spectroscopic data of the preferable complexes in aqueous solution, which are useful in the structural identification, have been presented.

2. Computational details

2.1. Determination of optimal structures and electronic transitions of 3-HCou species

Ground-state geometries for various 3-HCou species: non-protonated (neutral), protonated (cationic), deprotonated (anionic) and radical species were optimized in gas phase using DFT method with either the hybrid exchange-correlation functional B3LYP [36,37] in the *Gaussian 03* program [38] or the long-range-corrected functional CAM-B3LYP (i.e., Coulomb-Attenuating Method-B3LYP) [39,40] in the *Gaussian 09* program [41]. In recent years, B3LYP has become a standard functional used widely in the investigation of molecular structures, electronic transitions, excited states and spectroscopic properties of several coumarin-based molecules [34,42–46]. CAM-B3LYP can be regarded as an improved version of

B3LYP which allows better estimation of charge-transfer (CT) effect on the excitation energies in order to overcome the problem of traditional DFT of tending to underestimate CT-state energies [47]. The basis set 6-311++G(d,p) including a set of diffuse functions to the light atoms (such as hydrogen) was used for all calculations in this study, which was appropriate in cases where the proton-related phenomena such as deprotonation or proton-transfer reactions were of attention. No other basis sets were used as this study aimed at briefly examining applicability of the two hybrid functionals mentioned earlier in the prediction of UV/visible absorption, and also finding the most thermodynamically preferential pathway of complexation between 3-HCou and various metal ions. The optimal ground-state geometries were taken to the process of vibrational frequency calculations, where the zero-point corrected electronic energies and thermodynamic quantities were evaluated. Solvation effects were taken into account by repeating the full geometry optimizations under the integral-equation-formalism polarizable continuum model (IEFPCM) of solvation [48] at the same level of theory as used in the gas-phase optimizations. In the IEFPCM methodology, the solute molecule was placed in a theoretical cavity surrounded by a polarizable dielectric continuum of water (dielectric constant = 78.39). This theoretical cavity for solute was made from interconnecting spheres centered at the atomic positions of elements in the solute molecule. The radii of these spheres were defined according to the United Atom Kohn–Sham (UAKS) topological model. The vertical excitation energies responsible for the UV/visible absorption bands were determined by performing the Time-Dependent DFT (TD-DFT) calculations on the optimal ground-state geometries in solvated phase. In the search of the first excited-state structures of 3-HCou species in aqueous solution, the excited-state geometry optimizations with the CIS method at the IEFPCM/6–311++G(d,p) level were performed. Since the *Gaussian 03* program does not provide analytic energy gradients essential in optimizing the excited-state geometries within the pure DFT framework such as TD-DFT, Configuration Interaction Singles (CIS) method could be alternatively used. The single-point TD-DFT calculations at the IEFPCM/B3LYP/6-311++G(d,p) level were subsequently applied to the resulting CIS-optimized excited-state structures, allowing prediction of emission properties. We applied the TD-DFT calculations to determine the emission properties because no electron correlations were included in the CIS optimizations. In the previous work, the geometry optimizations with the CIS/6-31 + G(d) method were carried out to find the optimal excited-state structures of a coumarin-type laser dye molecule known as Coumarin 6; the emission wavelengths based on the PCM/TD-DFT computations on the CIS-optimized excited-state geometries satisfactorily reproduced the experimental values for such the dye in various solvents [42]. The CIS method with the SVPD basis set was formerly used to visualize electron density for the excited states of various 7-hydroxy-4-methylcoumarin species [34]. Nevertheless, in this work, emission properties in aqueous solutions of 3-HCou species were also examined within the IEFPCM/TD-DFT excited-state optimization methodology available in the *Gaussian 09* program, using the long-range-corrected

functional CAM-B3LYP. Absorption and emission wavelengths from the calculations were compared with those from the previous experiment. A number of benchmark calculations attempted by several groups suggested that TD-DFT methodology provided average accuracy of excitation energies within the range 0.2–0.3 eV for several organic compounds [49–53]. Jacquemin et al. [54] reported that PBE0 and CAM-B3LYP outperformed all other functionals in predicting the absorption wavelengths of many mono- and disubstituted coumarins based on the IEFPCM/TD-DFT calculations using the 6-311+G(2d,p) basis set. They also suggested that CAM-B3LYP was particularly well suited for treating molecules with delocalized excited states.

2.2. Natural bond orbital (NBO) analysis of 3-HCou species

NBO analysis is a method for optimally transforming molecular orbitals derived from DFT calculations into the localized forms of wavefunctions known as natural orbitals. In such the analysis, the bond orbitals are equivalent to the two-center NBO wavefunctions while the lone-pair or unpaired electron orbitals correspond to the one-center NBO wavefunctions. Based on the second-order perturbative approach, the NBO analysis also allows quantitative evaluation of pairwise donor–acceptor orbital interaction energies useful in characterizing particular interactions that are responsible for electron transfer or hydrogen bonding. The NBO analysis was previously reported as being effective in describing electronic effects in flavonols [55,56] and hydroxycoumarin-based compound [57]. In this work, the NBO analysis was performed on the most stable ground-state geometry for each species of 3-HCou using the *NBO 3.1* program available in the *Gaussian 03* program package.

2.3. Kinetic study of ground-state and excited-state IPT reactions

The transition-state structure formed during the IPT reaction of 3-HCou was determined based on the synchronous transit-guided quasi-Newton (STQN) method available in *Gaussian 03* using the QST2-calculation option. In such the option, the optimized structures of both reactant and product needed to be specified. For each of the geometries, the presence of a single imaginary vibrational frequency was an indication of being a transition state. The activation energy ($\Delta E^{\ddagger}$) of reaction was determined from the energy of the transition-state structure minus that of the reactant structure. According to the transition-state theory, the rate constant (k) of reaction at a given temperature T can be determined using the equation [58]:

$$k = \kappa \cdot \frac{k_B T}{h} \cdot \frac{Q^{TS}}{Q^R} \cdot \exp(-\Delta E^{\ddagger}/RT), \qquad (1)$$

where k_B is the Boltzmann constant, h the Planck constant, and R the gas constant. Q^{TS} and Q^R denote the total partition functions for the transition state and the reactant in the IPT reaction, respectively. The Wigner transmission coefficient [59], κ, which accounts for the barrier-tunneling correction, is given by:

$$\kappa = 1 + \frac{1}{24}\left(\frac{h\nu_i}{k_B T}\right)^2, \qquad (2)$$

where ν_i is the imaginary vibrational frequency at the saddle point. Eq. (2) was formerly applied to the theoretical approximation of rate constants of hydroperoxyl radical addition to various cyclic nitrones [60] and isomerization of benzothiazole derivatives [61].

2.4. Thermodynamic study of complexation and UV/visible absorption of complexes

Deprotonated (anionic) form of 3-HCou was treated as a bidentate ligand for complexation with various types of transition metal
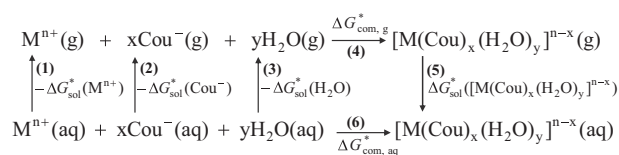
Scheme 2. Complexation in gas and aqueous phases, where M^{n+} and Cou$^-$ denote the transition metal ion and the deprotonated 3-HCou (ligand), respectively.

ions: Cr^{3+}, VO^{2+}, Zn^{2+} and Cu^{2+}. The deprotonated form was chosen as the ligand due to the fact that protonation at the donor O atoms could reduce the ability of electron donation to metal ion, to the extent that the metal chelation might be destabilized. The high negative charges for O1 and O3 in **Cou8** (see Table S3, Supplementary Materials) are ideal for metal-ion chelation. Also in terms of pharmacological applications, the superior water-solubility of the anionic (deprotonated) form would make it more preferable than the neutral (non-protonated) form. The gas-phase optimized structures of the complexes were explored using the same DFT computational level as that used for the pure ligand. In many recent researches, TD-DFT/B3LYP computations have been applied to predict the electronic spectra of several complexes formed by metal ions and coumarin-type ligands [43,62–65]. The TD-DFT single-point computations at the IEFPCM/B3LYP/6-311++G(d,p) level were performed on the gas-phase optimized structures of the complexes in the evaluation of UV/visible absorption in solution as well as the Gibbs energies of solvation. Structural changes upon solvation of the gas-phase optimized geometries were assumed to have negligible effects on the electronic transitions and the Gibbs energies, avoiding too expensive IEFPCM computations for large metal complexes. The mononuclear coordination was assumed in all cases. The metal-to-ligand (M: L) stoichiometric ratio was varied to find which ratio could lead to the most favorable complexation for each type of metal ion. Effects of coordinating water on the stability of complexes were also investigated. According to Scheme 2, at the 1 M standard state, the Gibbs energy of complexation in aqueous solution ($\Delta G^*_{\text{com, aq}}$) is related to its corresponding value in gas phase ($\Delta G^*_{\text{com, g}}$) through the equations:

$$\begin{aligned}
\Delta G^*_{\text{com, aq}} &= \Delta G^*_{\text{com, g}} + \Delta G^*_{sol}([\text{M(Cou)}_x\text{H}_2\text{O}_y]^{n-x}) - \Delta G^*_{sol}(\text{M}^{n+}) \\
&\quad - x\Delta G^*_{sol}(\text{Cou}^-) - y\Delta G^*_{sol}(\text{H}_2\text{O}) \qquad (3a) \\
&= \Delta G^*_{\text{com,g}} + \Delta\Delta G^*_{sol}
\end{aligned}$$

$$\Delta G^*_{\text{com, aq}} = \Delta G^{\circ}_{\text{com, g}} - RT \ln\left(\frac{C\tilde{R}T}{P^{\circ}}\right)(x+y) + \Delta\Delta G^*_{sol}, \qquad (3b)$$

where $\Delta G^*_{sol}([\text{M(Cou)}_x(\text{H}_2\text{O})_y]^{n-x})$, $\Delta G^*_{sol}(\text{M}^{n+})$, $\Delta G^*_{sol}(\text{Cou}^-)$ and $\Delta G^*_{sol}(\text{H}_2\text{O})$ are the Gibbs energies of solvation for the complex, metal ion, ligand and coordinating water, respectively; $R = 1.987 \times 10^{-3}$ kcal mol^{-1}, $T = 298.15$ K, $C = 1$ M, $\tilde{R} = 0.08206$ atm M^{-1} K^{-1} and $P^{\circ} = 1$ atm. The Gibbs energy of complexation in gas phase at 1 atm, $\Delta G^{\circ}_{\text{com, g}}$, is given by:

$$\begin{aligned}
\Delta G^{\circ}_{\text{com, g}} &= G^{\circ}_{g}((\text{M(Cou)}_x(\text{H}_2\text{O})_y)^{n-x}) - G^{\circ}_{g}(\text{M}^{n+}) \\
&\quad - xG^{\circ}_{g}(\text{Cou}^-) - yG^{\circ}_{g}(\text{H}_2\text{O}), \qquad (4)
\end{aligned}$$

where $G^{\circ}_{g}([\text{M(Cou)}_x(\text{H}_2\text{O})_y]^{n-x})$, $G^{\circ}_{g}(\text{M}^{n+})$, $G^{\circ}_{g}(\text{Cou}^-)$ and $G^{\circ}_{g}(\text{H}_2\text{O})$ are the absolute Gibbs energies in gas phase at 1 atm for the complex, metal ion, ligand and coordinating water, respectively.

Table 1
Molecular energies and thermodynamics of the ground-state geometries of 3-HCou species in aqueous solution.

Parameter	Neutral				Cation			Anion	Radical
	Cou1[a]	Cou2	Cou3	Cou4	Cou5[a]	Cou6	Cou7	Cou8	Cou9
Absolute molecular energy[b] [kcal mol^{-1}]									
E	−359,092.3	−359,085.4	−359,070.0	−359,057.0	−359,294.8	−359,293.9	−359,292.6	−358,757.4	−358,699.3
H	−359,086.2	−359,079.3	−359,064.1	−359,050.9	−359,288.5	−359,287.6	−359,286.4	−358,751.4	−358,693.2
G	−359,113.4	−359,106.8	−359,091.0	−359,078.4	−359,316.1	−359,315.2	−359,314.0	−358,778.8	−358,721.2
Relative molecular energy[c] [kcal mol^{-1}]									
E_{rel}	0	6.9	22.3	35.3	0	0.9	2.2	One form	One form
H_{rel}	0	6.9	22.1	35.3	0	0.9	2.1		
G_{rel}	0	6.6	22.4	35.0	0	0.9	2.1		
Thermodynamic energy[d] [kcal mol^{-1}]									
HBDE	79.4	57.2	72.5	44.1	–	–	–	–	–
ΔG^{*}_{sol}	−5.87	−11.8	−7.38	−16.7	−55.6	−56.4	−58.8	−56.2	−7.81

[a] The most stable geometries for a given species.
[b] E = Electronic energy with zero-point correction; H = enthalpy; G = Gibbs energy.
[c] All energies are relative to those of the most stable geometries.
[d] HBDE (homolytic bond dissociation enthalpy) = $H°$ ($H^{\bullet}$) + $H°$ (radical) − $H°$ (neutral), where radical = **Cou9**, neutral = **Cou1**, **Cou2**, **Cou3** or **Cou4** and $H^{\bullet}$ = hydrogen radical; ΔG^{*}_{sol} = standard Gibbs energy of solvation (1 M; 298.15 K).

3. Results and discussion

3.1. Optimal ground-state structures and stability

The optimal ground-state geometries with electrostatic potential (ESP) surfaces of the neutral (non-protonated), cationic (protonated), anionic (deprotonated) and radical species of 3-HCou in aqueous solution are illustrated in Fig. 1. The values of dihedral angles shown in Table S1 (Supplementary Materials) reveal that the fused benzene-pyrone skeleton in each of these optimal geometries is planar, indicating high degrees of electron delocalization over the two-ring structure. For the neutral species, four stable ground-state geometries labeled as **Cou1**, **Cou2**, **Cou3** and **Cou4** have been found and variation in the hydroxyl-group configuration is noticeable in this set of geometries. According to the relative energies shown in Table 1, the thermodynamic stability decreases in the order: **Cou1** > **Cou2** > **Cou3** > **Cou4**, hence suggesting that hydrogen bonding between O1 and H6 is crucial in acquiring high molecular stability. The difference in electronic energies between **Cou1** and **Cou2** is small (6.9 kcal mol^{-1}) as the transformation of **Cou1** to **Cou2** can be attained by only rotating the O3—H6 bond about the C7—O3 axis. The DFT computations also predict that protonation of the most stable neutral species prefers to take place at the oxygen atom O1 rather than O2, leading to the formation of three stable geometries for the cation. As seen in Fig. 1, the ground-state geometries of cation: **Cou5**, **Cou6** and **Cou7** form a group of conformers, with the stability decreasing in the order: **Cou5** > **Cou6** > **Cou7**. The electronic energy gap between **Cou7** and **Cou6** (1.3 kcal mol^{-1}) is wider than that between **Cou5** and **Cou6** (0.9 kcal mol^{-1}). Regarding the spatial orientation of O—H bonds in **Cou7**, the lack of intramolecular hydrogen bonding is the major cause of its low stability. The distance O3—H7 in **Cou5** (2.1697 Å) is slightly shorter than O1—H6 in **Cou6** (2.3393 Å), supporting that hydrogen bonding in the most stable conformer **Cou5** is stronger than that in the second most stable conformer **Cou6**. Deprotonation at the hydroxyl group in the neutral species allows the formation of anionic species while the release of hydrogen radical from the same hydroxyl group produces the radical species. As shown in Fig. 1, only one stable ground-state geometry has been found for either anion or radical. The electronic energy of the radical has been found to lie above that of the anion, yielding a relatively wide energy gap of 58.1 kcal mol^{-1}. As none of intramolecular hydrogen bond exists in either anion or radical, this finding reflects important roles of electron distribution in the geometry stabilization.

3.2. Orbital interactions, NBO atomic charges and electrostatic potential map

The donor–acceptor orbital interactions with the interaction energies for the most stable geometries: **Cou1**, **Cou5**, **Cou8** and **Cou9** are summarized in Table S2 (Supplementary Materials). The NBO atomic charges for these four geometries are shown in Table S3 (Supplementary Materials). The results from the NBO analysis of each species are described as follows.

Cou1 (neutral). As shown in Table S2, the bonding (BD) – antibonding (BD*) orbital interactions among the vicinal bonds: C1—C2, C3—C4 and C5—C9 are of considerable energies (18.2–21.8 kcal mol^{-1}). In pyrone ring, the interactions such as LP(O3)–BD*(C6—C7) (33.7 kcal mol^{-1}) and LP(O1)–BD*(O2—C8) (32.1 kcal mol^{-1}) are strong. These interactions ensure high degrees of electron delocalization. The markedly strong interactions: BD*(C5—C9)–BD*(C1—C2) and BD*(C5—C9)–BD*(C3—C4) suggest that BD*(C1—C2) and BD*(C3—C4) are strong electron acceptors. This result agrees well with either the ESP map (Fig. 1) where relatively high negative-charge densities are observed near the C1–C2–C3–C4 unit, or the negative NBO charges on C1 (−0.225), C2 (−0.180), C3 (−0.202) and C4 (−0.170). The interaction energies of the lone-pair (LP) orbitals suggest that electron-donating ability of O atoms follows as: LP(O2) > LP(O1) > LP(O3), being in line with the smallest and largest negative charges of −0.493 and −0.648 for O2 and O3, respectively. Most H atoms have similar charges of about +0.2, except H6 that is much more positively charged to +0.479, implying potential of H6 to be released as a proton. The hydrogen bond O1—H6 is stabilized through the interactions: LP(O1)–BD*(O3—H6) (2.55 kcal mol^{-1}), BD(C6—C7)–BD*(O3—H6) (1.22 kcal mol^{-1}) and BD(O3—H6)–BD*(C7—C8) (0.67 kcal mol^{-1}).

Cou5 (cation). The NBO charge on C2 becomes close to zero (Table S3), in accordance with the finding of almost uncharged region near C2 on the ESP map (Fig. 1). Significant decrease in the negative charges of C2, C3 and C4 upon protonation is caused by the strengthening of BD(C1—C2)–BD*(C5—C9) and BD(C3—C4)–BD*(C5—C9) associated with the decline in the interactions involving electron reception of BD*(C1—C2) and BD*(C3—C4). This effect is crucial in counteracting positive charge caused by protonation. The interactions LP(O2)–LP*(C8) and LP(O1)–LP*(H7) become more effective in withdrawing electrons from O2 and O1, causing the reduction in negative
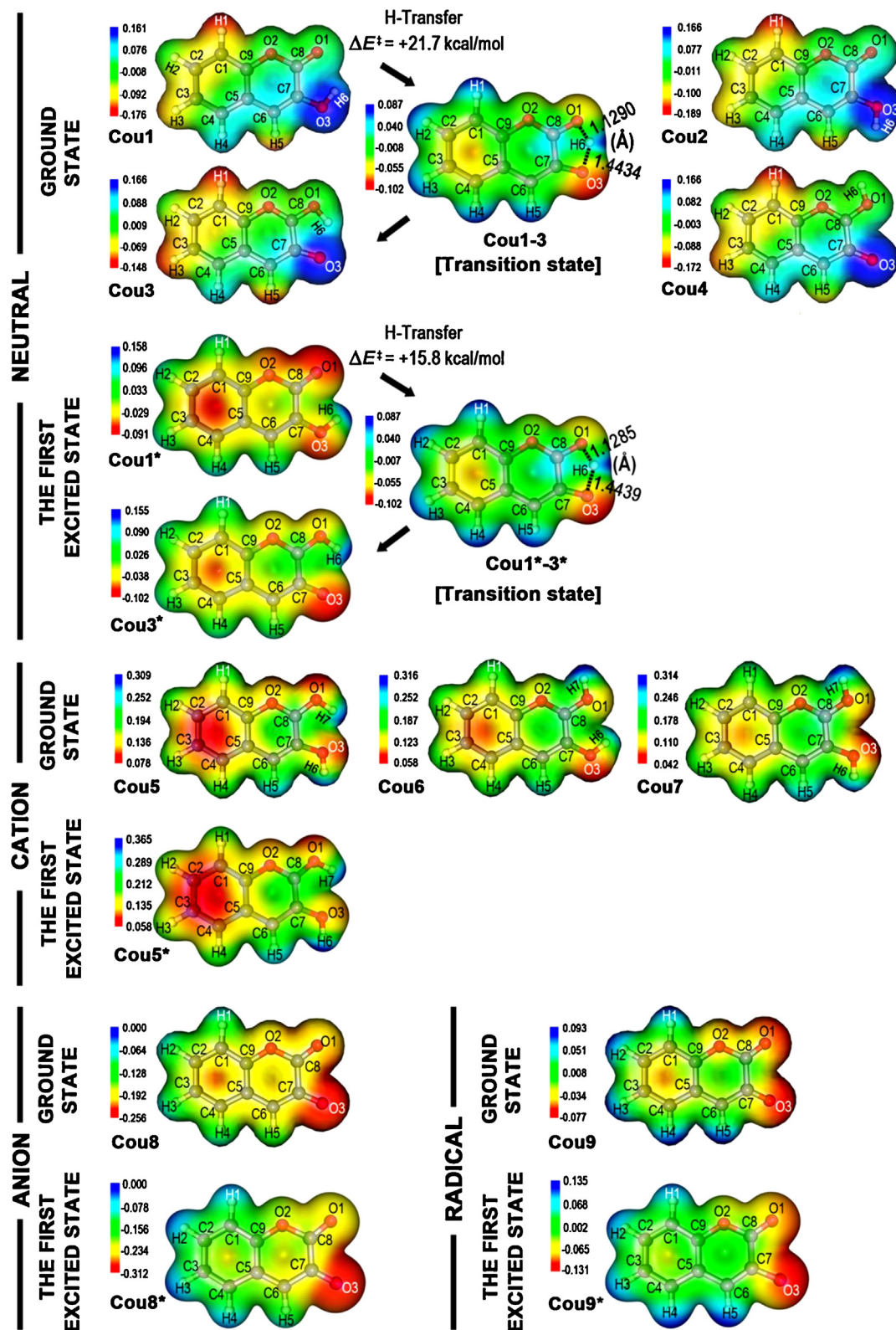
Fig. 1. Electrostatic potential (ESP) maps generated with isosurface value of 0.010e Å^{-3} for the optimized geometries of various 3-HCou species in aqueous solution. **Cou1**, **Cou2**, **Cou3** and **Cou4** denote the ground-state geometries of neutral (non-protonated) species. **Cou5, Cou6** and **Cou7** are the ground-state geometries of cationic (protonated) species. **Cou8** and **Cou9** are anionic (deprotonated) and radical species, respectively. The geometries marked with asterisks (*) are those of the first excited states. The reaction paths indicated by **Cou1** → **Cou1-3** (transition state) → **Cou3** and **Cou1*** → **Cou1*-3*** (transition state) → **Cou3*** represent intramolecular proton transfer (IPT) reactions in ground state and excited state, respectively. The activation energies ($\Delta E^{\ddagger}$) for both paths are included.

charges on both O atoms after protonation. The hydrogen bond O3—H7 in **Cou5** is stabilized by the interactions: LP(O3)–LP*(H7), BD(O3—H6)–LP*(H7), BD(O3—H6)–RY*(H7) and BD(C6—C7)–LP*(H7). As these interactions have low energies (see Table S2), the hydrogen bonding in the cation should be weaker than that in the neutral – this statement is true as the distance O3—H7 in **Cou5** (2.1687 Å) is longer than O1—H6 in **Cou1** (2.1211 Å). H6 and H7 have similarly large positive charges of 0.503 and 0.519, respectively. The repulsion between both H atoms and hydrogen bonding O3—H7 therefore cause the unique orientations of O1—H7 and O3—H6 seen in **Cou5**.

Cou8 (anion). Deprotonation eliminates the vicinal BD–BD* orbital interactions among C1—C2, C3—C4 and C5—C9, all of which use to be important in both **Cou1** (neutral) and **Cou5** (cation). This change reduces the extent of electron transfer from benzene to pyrone, most particularly through the weakening of BD(C5—C9)–BD*(C6—C7), hence allowing negative charges at the deprotonated site (O3) to be better stabilized. The new set of vicinal BD–BD* orbital interactions among C2—C3, C1—C9 and C4—C5 are formed, maintaining effective electron delocalization in benzene ring. The ESP maps reveal that the negative charge densities are distributed more uniformly in **Cou8** than either **Cou1** or **Cou5**. Particular interactions such as BD(C6—C7)–BD*(C8—O1), LP(O3)–BD*(C6—C7) and LP(O3)–BD*(C7—C8) become markedly strong, facilitating the transfer of negative charges from O3 to its neighborhoods. Similarly, the dramatically enhanced BD(C6—C7)–BD*(C4—C5) shift more electrons away from the vicinity of O3 toward benzene ring. The enhancement of LP(O2)–BD*(C1—C9) is very spectacular, with the interaction energy being almost 38 times its value in the neutral **Cou1** – this is interesting as deprotonation at O3 induce such a massive change to the interaction of orbitals far away from the deprotonated site.

Cou9 (radical). The same vicinal BD–BD* orbital interactions in benzene ring as found in the anion still remain in the radical; however the interaction energies are obviously lower for the radical. This implies decreased extent of electron delocalization in the radical that could lead to the weakening of UV/visible absorptivity. Most interactions in the radical show similar characters to those in the anion. For instance, BD(C6—C7)–BD*(C4—C5) and BD(C4—C5)–BD*(C6—C7) are, respectively, the most and second most influential benzene–pyrone orbital interactions in both **Cou8** and **Cou9**. Particular interactions in pyrone ring such as BD*(O2—C8)–BD*(C9—O2), BD(C7—O3)–BD*(C7—C8) and LP(O1)–BD*(C9—O2) are found only in the radical and anion. A comparison between the ESP maps of **Cou8** and **Cou9** (Fig. 1) shows that the negative charge densities across the two rings in the radical are clearly more distorted than in the anion, probably resulting from the weakening of many orbital interactions accounting for either electron transfer between the two rings or electron donation from the O atoms. Unlike the anion, the negative charge densities on O3 and O1 as seen on the ESP map for the radical are more comparable, in agreement with a small difference between the NBO charges of O3 (−0.459) and O1 (−0.499).

3.3. Gibbs energies of solvation and homolytic dissociation of hydroxyl group

Although the electronic energies of the conformers **Cou1** and **Cou2** of the neutral species are quite comparable to each other, the magnitudes of ΔG_{sol}^* for **Cou2** (−11.8 kcal mol^{-1}) and **Cou1** (−5.87 kcal mol^{-1}) are drastically different. On the other hand, ΔG_{sol}^* for **Cou1** lies closer to that for **Cou3** (−7.38 kcal mol^{-1}). This suggests that intramolecular hydrogen bonding present in **Cou1** and **Cou3** could possibly lead to limited degrees of hydration, hence yielding relatively small solute–solvent interaction

energy. This is well supported regarding the large magnitudes of ΔG_{sol}^* for such the conformers as **Cou2** and **Cou4**, where the intramolecular hydrogen bonding does not exist. Homolytic dissociation of the O–H bond in the neutral species, which allows the formation of hydrogen radical (H•) and the most stable radical species of 3-HCou (**Cou9**), can be schematically represented by: Neutral species → H• + **Cou9**. The enthalpy associated with such the bond dissociation, namely, the homolytic bond dissociation enthalpy (HBDE) is given by: HBDE = H° (H•) + H° (**Cou9**) − H° (Neutral species). According to Table 1, the large HBDE values for the conformers **Cou1** (79.4 kcal mol^{-1}) and **Cou3** (72.5 kcal mol^{-1}) as well as the much smaller HBDE values for the conformers **Cou2** (57.2 kcal mol^{-1}) and **Cou4** (44.1 kcal mol^{-1}) indicate that the intramolecular hydrogen bonding considerably hinders the homolytic O—H bond cleavage, hence limiting the extent of hydrogen radical production from both **Cou1** and **Cou3**.

3.4. Molecular orbitals and UV/visible absorption wavelengths of 3-HCou species

For the most stable forms of 3-HCou species, the highest occupied molecular orbital (HOMO) and the lowest unoccupied molecular orbital (LUMO) energies based on the geometries optimized with the IEFPCM/DFT method at the B3LYP/6-311++G(d,p) and CAM-B3LYP/6-311++G(d,p) levels are shown in Table 2. In both cases of B3LYP and CAM-B3LYP, the radical **Cou9** is predicted to be the best Lewis acid (electron acceptor) due to having the lowest-lying LUMO level. On the other hand, with the highest-lying HOMO level, the anion **Cou8** shows the highest tendency of being the Lewis base (electron donor). As shown in Fig. S1 (Supplementary Materials), excluding the radical, the MO energies are fitted well to the following linear relations: LUMO(B3LYP) = $−1.18n − 0.80$ [$R^2 = 0.9896$], HOMO(B3LYP) = $−1.27n − 4.81$ [$R^2 = 0.9845$], LUMO(CAM-B3LYP) = $−1.19n + 0.17$ [$R^2 = 0.9891$] and HOMO(CAM-B3LYP) = $−1.31n − 6.33$ [$R^2 = 0.9780$], where n is the number of hydrogen atoms bound to oxygen atoms: **Cou8** (anion, $n = 0$), **Cou1** (neutral, $n = 1$) and **Cou5** (cation, $n = 2$). Upon passing from B3LYP to CAM-B3LYP, the LUMOs are shifted upwards and the HOMOs downwards, thus widening the HOMO–LUMO gaps by about 2.6 eV for all species including the radical. Among all species, the radical **Cou9** has the narrowest HOMO–LUMO gap (i.e., the gap between L(β) and H(β) regarding only the orbitals with the same spin state). Based on the Koopman's theorem, the chemical hardness (η) is proportional to the HOMO–LUMO gap: $\eta = (E_L − E_H)/2$. The radical **Cou9** can be regarded as being highly polarizable or "soft" due to the narrow L(β)–H(β) gap, thus predicted to be more chemically reactive than the other species to the unimolecular reaction such as decomposition. The highest dipole moment in aqueous solution belongs to the anion **Cou8**; therefore this species should exhibit superior compatibility with polar solvent compared with the other species.

Numerical values of the Cartesian components of the ground-to-excited state transition electric dipole moments for the most stable 3-HCou species are shown in Table S4 (Supplementary Materials). The orientations of such the moments are defined according to the molecular axes given in Fig. S2 (Supplementary Materials). The UV/visible absorption wavelengths (λ_{abs}) in aqueous solution for **Cou1**, **Cou5**, **Cou8** and **Cou9** predicted based on the TD-DFT calculations are shown in Table 2 along with the experimental data reported by Wolfbeis [66]. The UV/visible absorption spectra based on the TD-DFT calculations of 3-HCou species are displayed in Fig. S3 (Supplementary Materials). As shown by the experiment–prediction correlation plot in Fig. 2, the predicted absorption wavelengths agree with the experimental ones. For the neutral species, whereas the functional CAM-B3LYP underestimates λ_{abs}'s (% error = 5 and 12%), using the functional B3LYP

Table 2
The HOMO/LUMO energies and UV/visible absorption properties in aqueous solution based on the IEFPCM/TD-DFT calculations of the ground-state geometries optimized at (A) B3LYP/6-311++G(d,p) and (B) CAM-B3LYP/6-311++G(d,p) levels of theory.

	(A) B3LYP/6-311++G(d,p)							(B) CAM-B3LYP/6-311++G(d,p)							λ_{abs} (exp)[g]
	E(L)[a]	E(H)[b]	ΔE(L-H)[c]	D[d]	λ_{abs}[e]	f[f]	MO contribution	E(L)[a]	E(H)[b]	ΔE(L-H)[c]	D[d]	λ_{abs}[e]	f[f]	MO contribution	
Cou1	−1.84	−6.26	4.42	4.18	299.6	0.403	H → L (79%)	−0.87	−7.87	7.00	5.16	283.7	0.462	H → L (95%)	322.3[h]
					276.5	0.009	H − 1 → L (80%); H → L+1 (15%)					252.3	0.017	H − 1 → L (67%); H → L+2 (26%)	266.5[h]
Cou5	−3.23	−7.25	4.02	5.26	341.0	0.182	H → L (69%); H − 1 → L (15%)	−2.27	−8.84	6.57	4.65	315.1	0.321	H → L (97%)	306.6[i]
					309.1	0.168	H − 1 → L (74%); H → L (10%)					284.2	0.068	H − 1 → L (93%)	290.5[i]
					236.8	0.112	H − 2 → L (43%); H → L+1 (43%)					219.1	0.186	H − 2 → L (10%); H − 1 → L+1 (15%); H → L+1 (45%); H → L+2 (12%)	235.3[i]
Cou8	−0.87	−4.72	3.85	12.1	342.7	0.380	H → L (77%)	0.10	−6.22	6.32	13.7	326.1	0.465	H → L (96%)	327.5[j]
					298.1	0.031	H → L+1 (82%)								
Cou9	−2.07 (α)[k]	−6.23 (α)[k]	4.16	9.48	601.5	0.008	H (β) → L (β) (100%)	−1.07 (α)[k]	−7.83 (α)[k]	6.76	10.5	487.1	0.014	H (β) → L (β) (93%)	–
	−4.16 (β)[k]	−7.22 (β)[k]	3.06		431.8	0.015	H − 2 (β) → L (β) (65%)	−3.18 (β)[k]	−8.88 (β)[k]	5.70		405.7	0.016	H (α) → L (α) (29%) H − 2 (β) → L (β) (57%)	

[a] LUMO energy in eV.
[b] HOMO energy in eV.
[c] HOMO–LUMO gap in eV.
[d] Dipole moments in Debye.
[e] Predicted absorption wavelengths in nm.
[f] Oscillator strengths.
[g] Experimental absorption wavelengths in nm taken from Ref. [66].
[h] Measured at pH = 7.61.
[i] Measured at pH = 3.12.
[j] Measured at pH = 10.02.
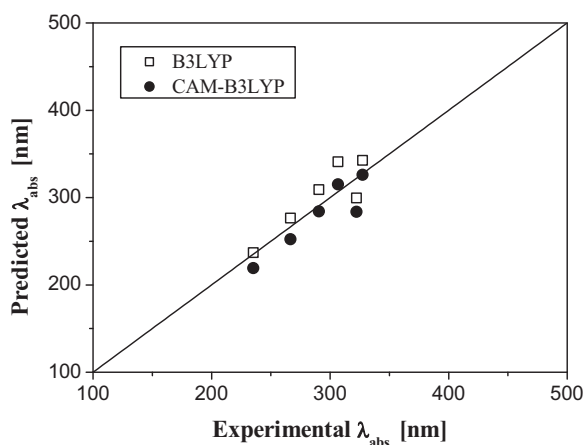[k] (α) = alpha-spin molecular orbital; (β) = beta-spin molecular orbital.

Fig. 2. UV/Visible absorption wavelengths (λ_{abs}) of 3-HCou species in aqueous solution: experiment vs. prediction with TD-DFT method using either B3LYP or CAM-B3LYP functionals.

provides more accurate λ_{abs}'s (% error = 4 and 7%). The larger deviation is noticed for the weaker absorption band (i.e., the one with the lower oscillator strength). The λ_{abs}'s for the neutral species are somehow underestimated with the CAM-B3LYP functional. This agrees with the previous benchmark-calculation study on a series coumarin–chalcone hybrids where CAM-B3LYP has been reported as tending to overcorrect CT excitation energies, yielding higher energies (shorter wavelengths) [47]. In the case of the charged species such as cation and anion, on the other hand, the CAM-B3LYP functional is more effective in predicting most of the experimental λ_{abs}'s, particularly the ones of the maximal absorption ($\lambda_{abs,max}$). Considering only the charged species, the functionals B3LYP and CAM-B3LYP yield the mean absolute errors for λ_{abs}'s of 17.4 nm

and 8.1 nm, respectively. Furthermore, based on the closeness of the experimental λ_{abs}'s for the neutral, anion and cation shown in Table 2, the presence of more than one species in a solution at a given pH would certainly result in significant degrees of band overlap, hence altering the absorption peaks. In this case, deconvolution of the experimental bands is very necessary for the precise species assignments, thus allowing better comparison with our calculations. The TD-DFT calculations reveal that the absorption maxima of all species are principally caused by the HOMO–LUMO transitions (H → L) based on the huge percentages of spectral contribution (see Table 2). Fig. 3 illustrates the spatial distributions of various MOs including the HOMOs and LUMOs for all 3-HCou species. It is worth mentioning that the shapes of HOMOs and LUMOs are somewhat independent of the choices of functional (B3LYP or CAM-B3LYP). **Cou1**, **Cou5** and **Cou8** show similar spatial distributions for either the HOMO or LUMO. The LUMO has nodes across the C1—C2, C3, C4—C5, C5—C9, C6—C7 and C8—O2 regions; however these regions are occupied in the case of HOMO. The transition H → L, which can be regarded as having the π → π* character, thus leads to marked alteration of the nodal patterns over benzene and pyrone rings, hence yielding high oscillator strength. For the cation **Cou5**, the other transitions with higher excitation energies become increasingly important (see Table 2); all of them still have the π → π* character. It is interesting to see that the transitions such as H − 1 → L and H − 1 → L + 1 for the cation also show a sign of charge transfer from benzene to pyrone moieties. For the radical **Cou9**, the spatial distribution of the HOMO is not much different from that of LUMO (only the beta-spin MOs of **Cou9** are shown in Fig. 3). As a result, the transition H → L in the radical would provide low oscillator strength in comparison with the same transition for the other species. The experimental data for the radical are not found but the calculations predict that this species is weakly absorptive in the visible region (the oscillator strengths up to only 0.016) and the strongest band is primarily assigned to the transition
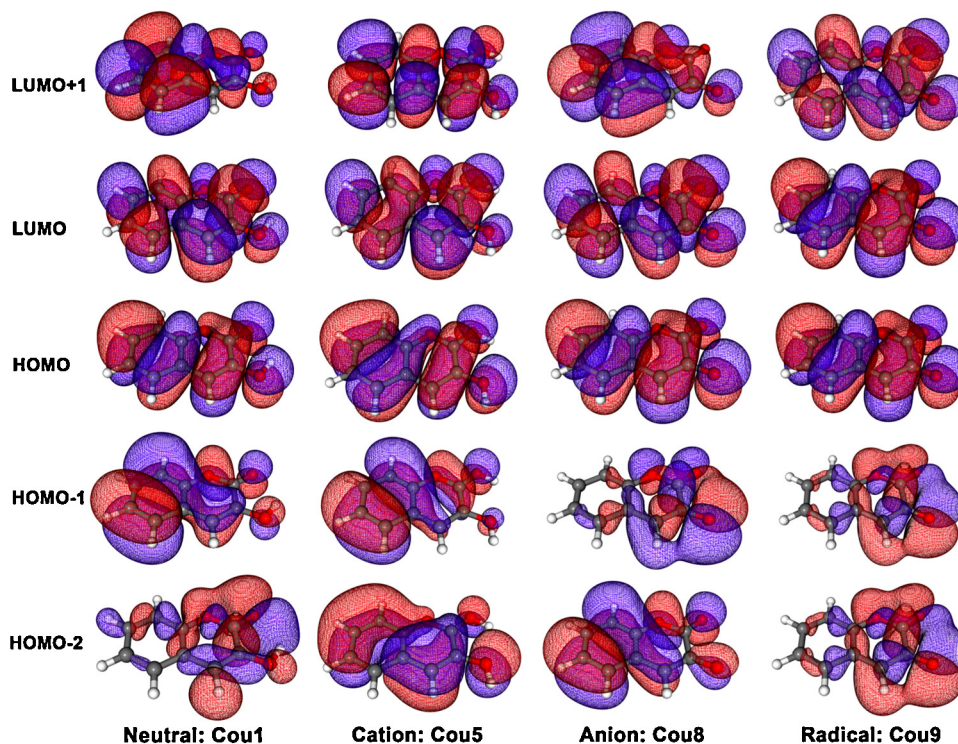

Fig. 3. Spatial distributions of selected molecular orbitals for **Cou1** (column 1), **Cou5** (column 2), **Cou8** (column 3) and **Cou9** (column 4), where HOMO = the highest occupied molecular orbital, HOMO − 1 = the second highest occupied molecular orbital, LUMO = the lowest unoccupied molecular orbital and LUMO + 1 = the second lowest occupied molecular orbital.

Table 3

Emission properties in aqueous solution of the first excited-state geometries optimized at **(1)** the IEFPCM/CIS/6-311++G(d,p) level and **(2)** the IEFPCM/DFT/CAM-B3LYP/6-311++G(d,p) level. All emission properties result from the TD-DFT calculations.

	λ_{em}[a]		f[b]		λ_{em}(exp)[c]	%Error for λ_{em}	
	(1)	(2)	(1)	(2)		(1)	(2)
Cou1*	340.0	336.3	0.445	0.483	380.0[d]	11	12
Cou5*	368.4	355.5	0.277	0.365	379.5[e]	3	6
Cou8*	374.0	379.8	0.417	0.479	Not available	–	–

[a] Predicted emission wavelengths in nm.
[b] Oscillator strengths.
[c] Emission wavelengths in nm taken from Ref. [66] (excitation wavelength = 318 nm).
[d] Measured at pH = 7.61.
[e] Measured at pH = 3.12.

$H - 2(\beta) \rightarrow L(\beta)$, exhibiting substantial amount of charge transfer from pyrone to benzene moieties.

3.5. Excited states and emission properties of 3-HCou species

For the first excited-state geometries: **Cou1*** (neutral), **Cou5*** (cation) and **Cou8*** (anion), the fluorescence emission is assigned to the vertical transition from the singlet excited state (S_1) to the singlet ground state (S_0). For the excited-state radical **Cou9***, the fluorescence emission corresponding to the vertical transition between its doublet states is negligible; the radical can basically be regarded as being non-fluorescent. Table 3 displays the emission properties derived from the first excited states of 3-HCou species using two different computational approaches: **(1)** IEFPCM/TD-DFT/B3LYP/6-311++G(d,p) single-point calculations of the excited-state geometries having been optimized at the IEFPCM/CIS/6-311++G(d,p) level and **(2)** IEFPCM/TD-DFT/CAM-B3LYP/6-311++G(d,p) single-point calculations of the excited-state geometries having been optimized at the IEFPCM/DFT/CAM-B3LYP/6-311++G(d,p) level. As shown in Table 3, the emission wavelengths (λ_{em}) corresponding to the minimal emission energies of the three emissive species: neutral (**Cou1***), cation (**Cou5***) and anion (**Cou8***) lie within the UV-A region, being red-shifted relative to the absorption wavelengths. For both types of the functional being used, the oscillator strengths of emission (f) are in the order: **Cou1*** > **Cou8*** > **Cou5***. Thus, the neutral species is predicted to be the strongest fluorophore, being in good agreement with the experiment [66]. The same experiment also indicates the quenching of emission intensity by OH⁻, being in line with our prediction. Theoretical approaches **(1)** and **(2)** clearly underestimate λ_{em}'s. However, the relative errors are fairly acceptable allowing for the fact that the presence of more than one emissive species in solution could complicate the experimental emission bands. Otherwise, the longer experimental λ_{em}'s may imply the low-lying excited states in the real system. Practically, alternative methods of excited-state calculations such as the multi-reference configuration interaction method or coupled cluster method may allow more accurate estimation of the emission wavelengths.

3.6. Ground-state and excited-state IPT reactions

Theoretical kinetic parameters for the IPT reactions of non-protonated 3-HCou are summarized in Table 4. As depicted in Fig. 1, **Cou1-3** specifically denotes the optimized transition-state (TS) geometry through which the transfer of proton (H6) from O3 to O1 accomplishes. Such the IPT essentially triggers the transformation of the most stable **Cou1** into its geometrical isomer **Cou3**. **Cou1-3** has exactly one imaginary vibrational frequency of $992.32i$ cm⁻¹, ensuring this geometry is the transition state. During the course of the TS formation, the elongation of the distance O3—H6 from 0.9720 Å in **Cou1** to 1.4434 Å in **Cou1-3** together with the accumulation of negative charges around O3

(see the ESP map of the TS, **Cou1-3**) assist in the O3—H6 bond dissociation. On the other hand, the distance O1—H6 is reduced from 2.1210 Å in **Cou1** to 1.1290 Å in **Cou1-3**, hence an indication of the O1—H6 bond formation. The following pathway of IPT: **Cou1** (ground) → **Cou1-3** (TS) → **Cou3** (ground) yields the activation energy ($\Delta E^{\ddagger}$) of 21.7 kcal mol⁻¹, which corresponds to the rate constant (k) at 298.15 K of 8.94×10^{-4} s⁻¹. Although the energy barrier is quite high, being about 37 times greater than the thermal energy RT (given $RT \approx 0.59$ kcal mol⁻¹ at 298.15 K), it is close to the theoretical energy barrier heights for the proton transfer reaction in 7-hydroxy-4-methylcoumarin (17–20 kcal mol⁻¹) [34,67]. In Fig. 1, **Cou1*** and **Cou3*** are the optimized excited-state geometries of **Cou1** and **Cou3**, respectively, obtained using approach **(1)** as described in Section 3.5. The ESP surfaces of **Cou1*** and **Cou3*** appear much different from those of the corresponding ground-state geometries. In the ESP map of **Cou1***, the slight negative charge densities appear distributed rather uniformly over the carbon–carbon interconnected structure, except for the three O atoms and the region close to the C2—C3—C4 segment on the inside of benzene ring that show markedly intense negative charge densities. The pathway: **Cou1*** (excited) → **Cou1*-3*** (TS) → **Cou3*** (excited) represents the excited-state IPT reaction, where **Cou1*-3*** is the optimized transition-state geometry. Excitation of the ground-state geometries usually induces the changes in either charge distributions or structural parameters, hence affecting the activation energy of reaction. As shown in Table, the excited-state reaction yields the activation energy of 15.8 kcal mol⁻¹, reduced from the ground-state value by 5.9 kcal mol⁻¹. Molecular excitation therefore leads to the 27% reduction in the activation energy, much increasing the rate of reaction. Nevertheless, the energy barrier in this case is still considerably high ($\approx 27RT$). Based on the structural parameters in Table S1, the two transition states: **Cou1*-3*** and **Cou1-3** are however not much different in terms of geometry; also the electronic energy gap between them is negligible (~ 0.002 kcal mol⁻¹) in accordance with the similarities in either their ESP surfaces (Fig. 1) or the parameters such as the partition functions and imaginary vibrational frequencies (Table 4). Thus, rather than the change in the electronic energy of the transition state, the increase in the electronic energy of the reactant upon

Table 4

Theoretical kinetic parameters for IPT reactions in aqueous solution: **(a)** The ground-state reaction: **Cou1 → Cou1-3 (TS) → Cou3**. **(b)** The excited-state reaction: **Cou1* → Cou1*-3* (TS) → Cou3***.

Parameter	(a)	(b)
Activation energy, $\Delta E^{\ddagger}$ [kcal mol⁻¹]	21.7	15.8
Total partition function of reactant, Q_{Rea}	2.52×10^{29}	6.43×10^{29}
Total partition function of transition state, Q_{TS}	1.40×10^{29}	1.41×10^{29}
Imaginary vibrational frequency of transition state, ν_i [cm⁻¹]	−992.32	−987.72
Wigner transmission coefficient, κ	1.96	1.95
Rate constant, k [s⁻¹]	8.94×10^{-4}	7.3

excitation is the major cause of the reduction in the activation energy. For the excited-state IPT reaction, the rate constant (k) is $7.3\,s^{-1}$, hence the excited-state IPT is predicted to be 8×10^3 times more rapid than the ground-state IPT.

3.7. Thermodynamics of complexation

Various possible complexation schemes for each type of metal ions together with the relevant reaction energies are presented in Table 5. In some cases, the same complexation schemes can give rise to different isomeric structures of the product (complex) labeled by the letters "**(a)**" and "**(b)**" in the product codes. The graphic representations in Fig. 4 clearly show that upon complexation, each ligand molecule uses two O atoms, i.e. O1 and O3, as donor atoms to chelate the metal ion, allowing five-membered chelate rings to be formed. The isomerization is caused by the change in the chelation configuration of the donor atoms in the chelate ring. On the basis that the most preferable complexation reaction is the one that has the lowest Gibbs energy of complexation in solution ($\Delta G^*_{com, aq}$), **CrL3(b)**, **VL2(b)**, **ZnL2W2(b)** and **CuL3(b)** depicted in Fig. 4 are regarded as the most preferable complexes for Cr^{3+}, VO^{2+}, Zn^{2+} and Cu^{2+}, respectively. This finding is in line with the complexation in gas phase based on the values of the Gibbs energies of complexation in gas phase ($\Delta G^\circ_{com, g}$). The degree of complex formation in aqueous solution follows the order: **CrL3(b)** [−350.2] > **CuL3(b)** [−216.4] > **VL2(b)** [−155.9] > **ZnL2W2(b)** [−104.9], where the values in the square brackets are the $\Delta G^*_{com, aq}$ values in kcal mol^{-1}.

Furthermore, based on the distinctively low $\Delta G_{com, aq}$ value at −350.2 kcal mol^{-1}, **CrL3(b)** shows uniquely large extent of formation in comparison with the other complexes formed by Cr^{3+}. All $\Delta\Delta G^*_{sol}$ values are very large and positive as the solute–solvent interactions for the isolated metal ion and ligand molecules (the reactants) are much greater than those for complex (the product). The level of solute–solvent interactions decreases in the order: **CuL3(b)** [−43.5] > **ZnL2W2(b)** [−16.8] > **VL2(b)** [−7.67] > **CrL3(b)** [−7.25], where the values in the square brackets are the Gibbs energies of solvation (ΔG^*_{sol}) in kcal mol^{-1}. This finding is quite reasonable as **CuL3(b)** has the total charge of −1 whereas the other preferable complexes are uncharged. However, it was previously suggested that, in the PCM methodology, more solute charge could escape from the cavity for ionic solutes than for neutral solutes due to the exponential decay of electronic tails, hence providing limited accuracy of the computed Gibbs energy of solvation [68].

There are relatively large number of complexes which can be formed by Zn^{2+} and Cu^{2+}, obviously due to the diversity of water coordination schemes possible for both types of metal ions. On the other hand, for either Cr^{3+} or VO^{2+}, there are fewer possible complexes since the coordination by water molecules, in several cases, leads to the increase in the Gibbs energy of complexation relative to the most preferable one, hence lowering the degree of complexation. For either Cr^{3+} or Cu^{2+}, the most preferable complexation reactions can be achieved at the metal-to-ligand mole ratio (M: L) of 1: 3, yielding the six-coordinate complexes [**CrL3(b)** and **CuL3(b)**] with slightly distorted octahedral coordination geometries as

Table 5
Proposed complexation schemes with related reaction energies.

Complexation	Product code	N^b	ΔG^*_{sol} (complex)	Reaction energy [kcal mol^{-1}]						
				Gas phase				Aqueous solution		
				$\Delta E^\circ_{com, g}$	$\Delta H^\circ_{com, g}$	$\Delta G^\circ_{com, g}$	$\Delta G^\circ_{com, g}$ (rel)^c	$\Delta\Delta G^*_{sol}$	$\Delta G^*_{com, g}$	$\Delta G^*_{com, aq}$ (rel)^c
Chromium(III)										
$Cr^{3+} + L^- \rightarrow CrL^{2+}$	**CrL**	2	*Unstable*	–	–	–	–	–	–	–
$Cr^{3+} + L^- + 4H_2O \rightarrow [CrL(H_2O)_4]^{2+}$	**CrLW4**	6	−185.5	−935.1	−939.8	−888.0	427.4	707.6	−189.9	160.3
$Cr^{3+} + 2L^- + 2H_2O \rightarrow [CrL_2(H_2O)_2]^+$	**CrL2W2(a)**	6	−57.8	−1241.1	−1243.8	−1199.8	115.6	877.8	−329.6	20.6
$Cr^{3+} + 2L^- + 2H_2O \rightarrow [CrL_2(H_2O)_2]^+$	**CrL2W2(b)**	6	−49.4	−1244.3	−1246.8	−1203.5	111.9	886.2	−324.9	25.3
$Cr^{3+} + 3L^- \rightarrow CrL_3$	**CrL3(a)**	6	−8.71	−1031.5	−1032.5	−996.1	319.3	969.4	−32.4	317.8
$Cr^{3+} + 3L^- \rightarrow CrL_3$	**CrL3(b)**^{a}	6	−7.25	−1351.3	−1352.6	−1315.4	0.0	970.9	−350.2	0.0
Oxovanadium(IV)										
$VO^{2+} + L^- \rightarrow [(VO)L]^+$	**VL**	2	−68.3	−434.2	−435.1	−422.7	174.7	328.5	−96.1	59.8
$VO^{2+} + L^- + 2H_2O \rightarrow [(VO)L(H_2O)_2]^+$	**VLW2**	4	−55.9	−519.1	−521.4	−489.0	108.4	354.5	−140.1	15.8
$VO^{2+} + 2L^- \rightarrow (VO)L_2$	**VL2(a)**	4	−8.55	−621.1	−622.0	−596.4	1.0	444.4	−155.8	0.1
$VO^{2+} + 2L^- \rightarrow (VO)L_2$	**VL2(b)**^{a}	4	−7.67	−622.1	−623.0	−597.4	0.0	445.3	−155.9	0.0
Zinc(II)										
$Zn^{2+} + L^- \rightarrow ZnL^+$	**ZnL**	2	−93.1	−315.4	−316.6	−306.1	292.6	355.2	47.2	152.1
$Zn^{2+} + L^- + 2H_2O \rightarrow [ZnL(H_2O)_2]^+$	**ZnLW2**	4	−64.4	−391.5	−394.4	−363.8	234.9	397.5	28.1	133.0
$Zn^{2+} + L^- + 4H_2O \rightarrow [ZnL(H_2O)_4]^+$	**ZnLW4**	6	−57.8	−422.7	−426.6	−376.8	221.9	417.7	31.5	136.4
$Zn^{2+} + 2L^- \rightarrow ZnL_2$	**ZnL2(a)**	4	−16.2	−601.8	−602.9	−579.6	19.1	488.2	−95.2	9.7
$Zn^{2+} + 2L^- \rightarrow ZnL_2$	**ZnL2(b)**	4	−15.9	−603.4	−604.6	−581.0	17.7	488.6	−96.2	8.7
$Zn^{2+} + 2L^- + 2H_2O \rightarrow ZnL_2(H_2O)_2$	**ZnL2W2(a)**	6	−15.8	−636.1	−637.6	−596.8	1.9	502.3	−102.0	2.9
$Zn^{2+} + 2L^- + 2H_2O \rightarrow ZnL_2(H_2O)_2$	**ZnL2W2(b)**^{a}	6	−16.8	−637.4	−638.7	−598.7	0.0	501.3	−104.9	0.0
$Zn^{2+} + 3L^- \rightarrow ZnL_3^-$	**ZnL3(a)**	6	−44.6	−355.0	−355.2	−321.3	277.4	516.1	189.1	294.0
$Zn^{2+} + 3L^- \rightarrow ZnL_3^-$	**ZnL3(b)**	6	−44.7	−354.7	−354.9	−321.1	277.6	515.9	189.2	294.1
Copper(II)										
$Cu^{2+} + L^- \rightarrow CuL^+$	**CuL**	2	−51.5	−357.3	−357.8	−349.2	294.4	312.5	−38.6	177.8
$Cu^{2+} + L^- + 2H_2O \rightarrow [CuL(H_2O)_2]^+$	**CuLW2**	4	−55.3	−427.0	−429.3	−399.9	243.7	322.4	−83.2	133.2
$Cu^{2+} + L^- + 4H_2O \rightarrow [CuL(H_2O)_4]^+$	**CuLW4**	6	*Unstable*	–	–	–	–	–	–	–
$Cu^{2+} + 2L^- \rightarrow CuL_2$	**CuL2(a)**	4	−9.20	−636.8	−637.7	−615.2	28.4	411.0	−207.9	8.5
$Cu^{2+} + 2L^- \rightarrow CuL_2$	**CuL2(b)**	4	−8.98	−637.3	−638.2	−615.5	28.1	411.2	−208.1	8.3
$Cu^{2+} + 2L^- + 2H_2O \rightarrow CuL_2(H_2O)_2$	**CuL2W2(a)**	6	−15.2	−657.9	−659.0	−619.6	24.0	418.7	−208.5	7.9
$Cu^{2+} + 2L^- + 2H_2O \rightarrow CuL_2(H_2O)_2$	**CuL2W2(b)**	6	−17.8	−659.8	−661.4	−621.1	22.5	416.1	−212.6	3.8
$Cu^{2+} + 3L^- \rightarrow CuL_3^-$	**CuL3(a)**	6	−43.6	−371.8	−371.9	−338.9	304.7	432.8	88.2	304.6
$Cu^{2+} + 3L^- \rightarrow CuL_3^-$	**CuL3(b)**^{a}	6	−43.5	−677.1	−677.2	−643.6	0.0	432.9	−216.4	0.0

^{a} Complex resulting from the most preferable complexation.
^{b} Coordination number.
^{c} $\Delta G^*_{com, g}$ (rel) = [$\Delta G^*_{com, g}$ for a given complexation] − [$\Delta G^*_{com, g}$ for the most preferable complexation]; $\Delta G^*_{com, aq}$ (rel) = [$\Delta G^*_{com, aq}$ for a given complexation] − [$\Delta G^*_{com, aq}$ for the most preferable complexation].
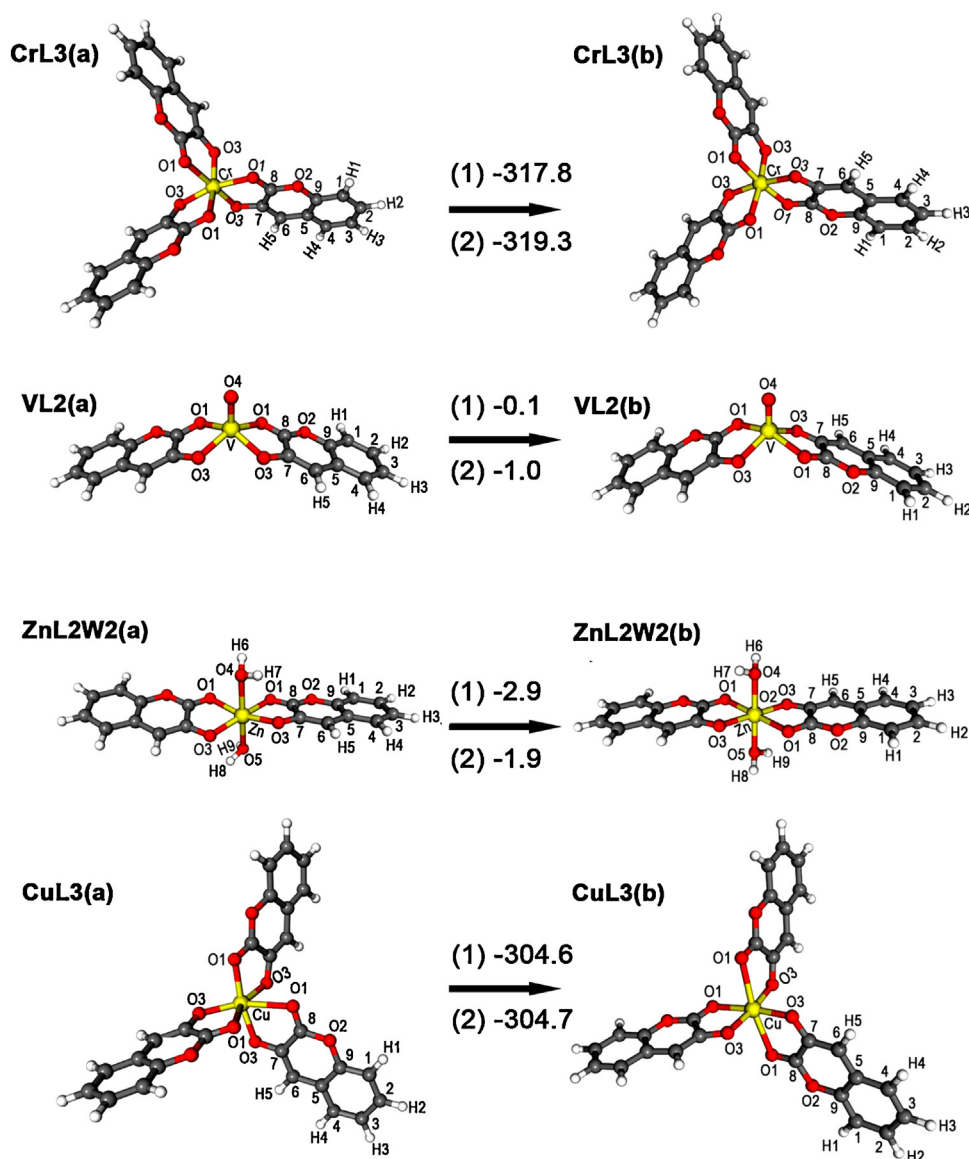
Fig. 4. Isomerization of the complexes formed by deprotonated 3-HCou and various transition metal ions: Cr^{3+} (row 1), VO^{2+} (row 2), Zn^{2+} (row 3) and Cu^{2+} (row 4). In each reaction (row), the most preferable complex is the product and its geometrical isomer the reactant. Standard Gibbs energies (in kcal mol^{-1}) for the isomerization in aqueous solution and gas phase are provided in (**1**) and (**2**), respectively.

illustrated in Fig. 4. For Zn^{2+}, formation of six-coordinate complex **ZnL2W2(b)** is most favorable; however, in this case, two molecules of coordinating water are required in the formation of octahedral coordination sphere. Removal of two coordinating water molecules from **ZnL2W2(b)** and **ZnL2W2(a)** produces the less preferable complexes **ZnL2(b)** and **ZnL2(a)**, respectively. Regarding the change in the Gibbs energies of complexation, coordination by two water molecules is crucial in acquiring high degrees of complexation for Zn^{2+}. The most preferable complex of VO^{2+} [**VL2(b)**] is formed at the M: L ratio of 1: 2, without any participation of coordinating water molecules. As a result, such the oxovanadium complex distinctively exhibits distorted square-pyramidal geometry of coordination as seen in Fig. 4. The isomerization reactions: **CrL3(b)** → **CrL3(a)** and **CuL3(b)** → **CuL3(a)** as depicted in Fig. 4 lead to the notable decrease in the Gibbs energies by 317.8 and 304.6 kcal mol^{-1}, respectively. The Gibbs energy decreases are markedly large because these isomerization reactions correspond to the transformation of the most preferable complex into the least preferable one. In contrast, based on the relative Gibbs energies of complexation in Table 5, the isomers **VL2(a)** and **VL2(b)**

exhibit comparable degrees of formation, similar to the case of the isomers **ZnL2W2(a)** and **ZnL2W2(b)**. The isomerization reactions: **VL2(b)** → **VL2(a)** and **ZnL2W2(b)** → **ZnL2W2(b)** involve with tiny changes in the Gibbs energies by 0.1 and 2.9 kcal mol^{-1}, respectively; hence, the change in the configuration of donor atoms (from *cis* to *trans*) in the two chelate rings (see Fig. 4) does not much affect the degree of complexation, most particularly for VO^{2+}.

3.8. UV/visible absorption of most preferable complexes and their geometrical isomers

UV/visible absorption spectra of the most preferable complexes and their corresponding geometrical isomers derived from the IEFPCM/TD-DFT/B3LYP/6-311++G(d,p) calculations are shown in Fig. 5. As seen in Fig. 5(A), the spectrum of **CrL3(b)** (the most preferable form) is obviously different from that of **CrL3(a)** (the least preferable form). The spectrum of **CrL3(b)** displays the most intense band at 449.3 nm assigned to the major transitions: $H - 1(\beta) \to L(\beta)$ (65%) and $H - 1(\beta) \to L + 3(\beta)$ (11%) with the oscillator strength of 0.1399 (see Table S5, Supplementary Materials);
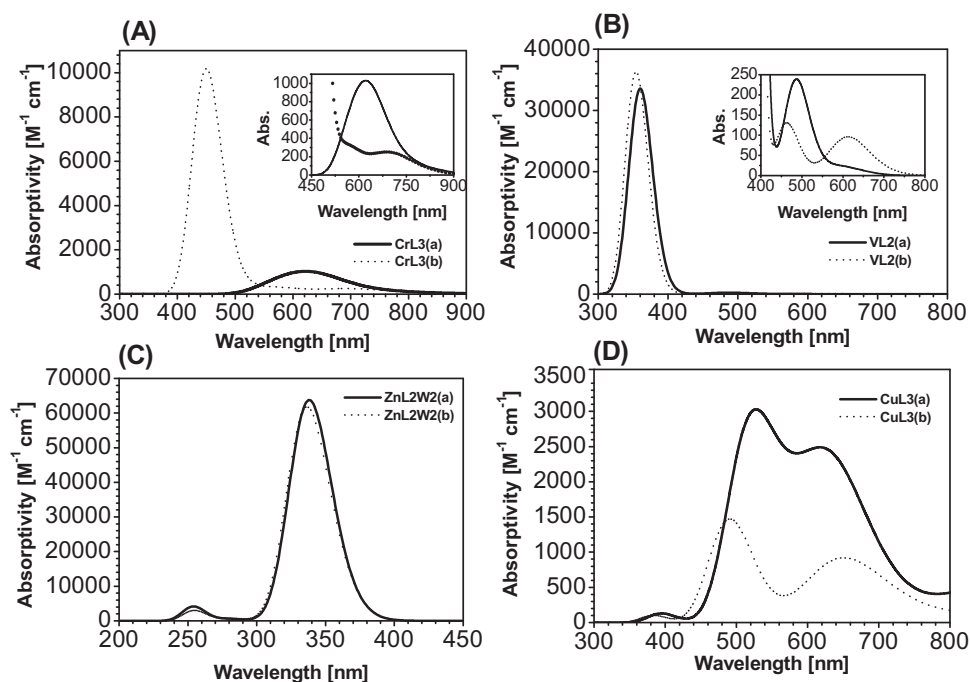
Fig. 5. UV/visible absorption spectra in aqueous solution theoretically predicted for the most preferable complexes and their geometrical isomers: (A) **CrL3(a)/CrL3(b)**, (B) **VL2(a)/VL2(b)**, (C) **ZnL2W2(a)/ZnL2W2(b)** and (D) **CuL3(a)/CuL3(b)**.

however, such the strong band is missing in the spectrum of **CrL3(b)**. For both **CrL3(a)** and **CrL3(b)**, the bands in the long-wavelength region (500–800 nm) are weak and broad. The weak absorption at 565.4 nm ($f=0.0017$) gives rise to a shoulder band next to the strongest band in the spectrum of **CrL3(b)**. A combination of two closely lying maxima at 681.6 nm ($f=0.0023$) and 735.5 nm ($f=0.0013$) produces a weak broad band near 690 nm, which is not well resolved from the shoulder band mentioned previously. In the case of **CrL3(a)**, there is only a single broad band with the maximum near 620 nm and this band essentially results from several absorption maxima at 646.9 nm ($f=0.0056$), 626.5 nm ($f=0.0061$), 565.8 nm ($f=0.0017$) and 573.5 nm ($f=0.0040$). In panel (B), the spectra of **VL2(a)** and **VL2(b)** are similar to each other regarding the presence of a markedly strong band near 360 nm, corresponding to the transitions: $H(\alpha)\rightarrow L(\alpha)$ ($\approx$50%) and $H(\beta)\rightarrow L(\beta)$ ($\approx$30%), with $f\approx0.4$. However, the band at 486.3 nm for **VL2(a)** ($f=0.0033$) is clearly stronger than the band at 462.7 nm for **VL2(b)** ($f=0.0018$). The emergence of a band at 614.2 nm is found to be a characteristic of the isomer **VL2(b)**. Since both **VL2(a)** and **VL2(a)** show very comparable extent of formation according to the thermodynamic data; therefore observation of mixed spectral features of both isomers may be possible in terms of experiment. In panel (C), the spectra of **ZnL2W2(a)** and **ZnL2W2(b)** show nearly indistinguishable appearance, with a remarkably strong band near 340 nm and a much weaker band at a short UV-wavelength of 250 nm. The strong band is ascribed to a combination of three absorption maxima in the range 280–350 nm, where the spectral contribution of the transition $H-1\rightarrow L+1$ predominates. The weak band is relatively narrow, resulting from two overlapping maxima at about 253 nm and 256 nm for either **ZnL2W2(a)** or **ZnL2W2(b)** (Table S5). No absorption bands are found in the visible region; hence the aqueous solution of both isomeric zinc(II) complexes should be colorless. In panel (D), the spectra of **CuL3(a)** and **CuL3(b)** display similar characters: (i) two strong bands overlapping in the range 430–800 nm and (ii) a broad band in the region of wavelengths shorter than 430 nm. However, there are major differences in both the intensities and the maxima of two strong

bands. According to the absorption calculations, the weak bands at 393.3 nm for **CuL3(a)** and at 382.2 nm for **CuL3(b)** originate from the transition $H(\alpha)\rightarrow L(\alpha)$ (>90%), with low oscillator strength values at about 0.001. In the spectrum of **CuL3(b)** (the most preferable complex), the primary strong band at 486.5 nm ($f=0.0153$) is assigned to the transition $H-1(\beta)\rightarrow L(\beta)$ (42%). The secondary strong band at 641.4 nm ($f=0.0098$) caused by the transition $H(\beta)\rightarrow L(\beta)$ (77%) is rather well separated from the primary band. Compared with the spectrum of **CuL3(b)**, the primary band in the spectrum of **CuL3(a)** appears at the longer wavelength of 531.5 nm and this band is assigned to $H-2(\beta)\rightarrow L(\beta)$ (46%), with the greater oscillator strength value at 0.0203. In contrast, the secondary strong band in the case of **CuL3(a)** is found at the shorter wavelength of 620 nm. Such the band is a result of combined absorption maxima at 635.8 nm ($f=0.0261$), 609.4 nm ($f=0.0054$) and 575.7 nm ($f=0.0021$), each of which corresponds to various transition contributions as shown in Table S5. All theoretically predicted results described in this section need to be verified by the experiment.

4. Conclusions

Regardless of the interaction energies, electron displacement within benzene ring for neutral and cationic species shows similar characteristics. Electron densities are essentially more localized over benzene ring than pyrone ring for both neutral and cationic species according to the electrostatic potential maps and NBO charges on carbon atoms. For the anionic species, based on the NBO analysis, alternation of the interacting pi-electron orbitals in benzene ring occurs as a result of negative charge at the deprotonation site in pyrone ring. The pyrone-to-benzene electron displacement is more favorable in the anionic species, causing the overall electron densities on the two rings (except on the O atoms) to become comparable. Anionic and radical species share similarity in terms of orbital-interaction characteristics; however the extent of electron displacement in the anionic species is much greater than that in the radical species. The hydrogen bond in the neutral species is stronger than that in the cationic species.

The stability of hydrogen bonding can be described in terms of the orbital interaction energies. Intramolecular hydrogen bonding enhances the structural stability but simultaneously restricts the release of proton or hydrogen radical from the hydroxyl group. The IPT reaction is responsible for the transformation of the most stable form of the neutral species into its isomeric form. The activation energy of such the reaction at 298.15 K in the ground state is predicted to be 21.7 kcal mol^{-1}. Upon excitation, the activation energy is reduced to 15.8 kcal mol^{-1}, making the IPT reaction much more kinetically favorable. TD-DFT calculations predicts that the HOMO–LUMO transitions (H $\rightarrow$ L) with $\pi \rightarrow \pi^*$ character principally account for the UV absorption in aqueous solution of the neutral, anionic and cationic species. The radical species are weakly absorptive in the visible region, with the major absorption band resulting from H(β) $- 2 \rightarrow$ L(β). The wavelengths at the absorption maxima ($\lambda_{abs,max}$) predicted based on the TD-DFT method for the neutral, cation and anion in solution are in agreement with the experiment. Using the functional B3LYP yields more accurate $\lambda_{abs,max}$ of the neutral species, whereas for the charged species the better agreement in $\lambda_{abs,max}$'s can be obtained with the long-range-corrected functional CAM-B3LYP. Varying the basis sets has not been attempted but it could allow better estimation of λ_{abs}. Reproducing the experimental absorption wavelengths for 3-HCou is rather tricky as the distribution of more than one absorptive species in solution at a given pH could modify the band positions. Deconvolution analysis of the experimental absorption bands is required in order to make a more reliable comparison with the calculations. TD-DFT calculations also show that the neutral species is the most emissive species and the formation of anion upon deprotonation leads to the reduction in emission intensity – these theoretical findings are well supported by the previous experimental evidences [66]. The most preferable complexation reactions in aqueous solution have been predicted and the resulting thermodynamic calculations indicate that Cr^{3+} shows the highest preference of complexation with the bidentate, deprotonated 3-HCou ligand (anionic species), followed by Cu^{2+}, VO^{2+} and Zn^{2+} in sequence. Also, the most preferable form of the chromium(III) complex (M:L = 1:3) apparently predominates the other possible forms. For either Cu^{2+} or Zn^{2+}, there are various forms of complexes with comparable degrees of formation in solution. In the case of oxovanadium(IV) and zinc(II) complexes, two isomers (M:L = 1:2) show distinguishingly high degrees of formation compared with the other forms, indicating preferential co-existence of both isomers in aqueous solution. Experimental evidences are essential in supporting all of these theoretical predictions for the complexes.

Acknowledgement

Appendix A. Supplementary data

Supplementary data associated with this article can be found, in the online version, at http://dx.doi.org/10.1016/j.jmgm.2014.04.009.

References

[1] J.R.S. Hoult, M. Payá, Gen. Pharmacol. Vasc. Syst. 27 (1996) 713–722.
[2] M. Payá, B. Halliwell, J.R.S. Hoult, Biochem. Pharmacol. 44 (1992) 205–214.
[3] S. Stanchev, V. Hadjimitova, T. Traykov, T. Boyanov, I. Manolov, Eur. J. Med. Chem. 44 (2009) 3077–3082.
[4] F. Bailly, C. Maurin, E. Teissier, H. Vezin, P. Cotelle, Bioorg. Med. Chem. 12 (2004) 5611–5618.
[5] M. Grazul, E. Budzisz, Coord. Chem. Rev. 253 (2009) 2588–2598.
[6] L. Du, M. Li, S. Zheng, B. Wang, Tetrahedron Lett. 49 (2008) 3045–3048.
[7] A. Lacy, R. O'Kennedy, Curr. Pharm. Des. 10 (2004) 3797–3811.
[8] B. Ramesh, K.V. Pugalendi, Life Sci. 79 (2006) 306–310.
[9] B. Ramesh, P. Viswanathan, K.V. Pugalendi, Eur. J. Pharmacol. 566 (2007) 231–239.
[10] J.F. Vasconcelos, M.M. Teixeira, J.M. Barbosa-Filho, M.F. Agra, X.P. Nunes, A.M. Giulietti, R. Ribeiro-dos-Santos, M.B.P. Soares, Eur. J. Pharmacol. 609 (2009) 126–131.
[11] M. Formica, V. Fusi, L. Giorgi, M. Micheloni, Coord. Chem. Rev. 256 (2012) 170–192.
[12] B. Abrams, Z. Diwu, O. Guryev, S. Aleshkov, R. Hingorani, M. Edinger, R. Lee, J. Link, T. Dubrovsky, Anal. Biochem. 386 (2009) 262–269.
[13] L. Wang, D. Ye, D. Cao, Spectrochim. Acta Mol. Biomol. Spectrosc. 90 (2012) 40–44.
[14] A.K. Mahapatra, K. Maiti, P. Sahoo, P.K. Nandi, J. Lumin. 143 (2013) 349–354.
[15] H. Kashida, K. Yamaguchi, Y. Hara, H. Asanuma, Bioorg. Med. Chem. 20 (2012) 4310–4315.
[16] R.A. Anderson, Diabetes Metab. 26 (2000) 22–27.
[17] R.A. Anderson, J. Am. Coll. Nutr. 17 (1998) 548–555.
[18] J.B. Vincent, Polyhedron 20 (2001) 1–26.
[19] Y. Adachi, Y. Yoshikawa, H. Sakurai, Biofactors 29 (2007) 213–223.
[20] H. Sakurai, Y. Kojima, Y. Yoshikawa, K. Kawabe, H. Yasui, Coord. Chem. Rev. 226 (2002) 187–198.
[21] M. Yamaguchi, K. Wakasugi, R. Saito, Y. Adachi, Y. Yoshikawa, H. Sakurai, A. Katoh, J. Inorg. Biochem. 100 (2006) 260–269.
[22] Y. Yoshikawa, E. Ueda, K. Kawabe, H. Miyake, T. Takino, H. Sakurai, Y. Kojima, J. Biol. Inorg. Chem. 7 (2002) 68–73.
[23] J. Jansen, W. Karges, L. Rink, J. Nutr. Biochem. 20 (2009) 399–417.
[24] M. Qazzaz, R. Abdul-Ghani, M. Metani, R. Husein, A.L. Abu-Hijleh, A.S. Abdul-Ghani, Biol. Trace Elem. Res. 154 (2013) 88–96.
[25] X.Z. Chen, Y.F. Niu, W.P. Liu, L. Li, Y.T. Wang, Y.R. Li, W.G. Gao, Y. Yu, Acta Chim. Sin. 64 (2006) 879–883.
[26] S. Sitasawad, M. Deshpande, M. Katdare, S. Tirth, P. Parab, Diabetes Res. Clin. Pract. 52 (2001) 77–84.
[27] H. Sakurai, Chem. Rec. 2 (2002) 237–248.
[28] G.R. Willsky, A.B. Goldfine, P.J. Kostyniak, J.H. McNeill, L.Q. Yang, H.R. Khan, D.C. Crans, J. Inorg. Biochem. 85 (2001) 33–42.
[29] D. Malesev, V. Kuntic, J. Serb. Chem. Soc. 72 (2007) 921–939.
[30] W. Basuki, M. Hiromura, H. Sakurai, J. Inorg. Biochem. 101 (2007) 692–699.
[31] H. Haase, W. Maret, Biometals 18 (2005) 333–338.
[32] I. Kostova, I. Manolov, I. Nicolova, S. Konstantinov, M. Karaivanova, Eur. J. Med. Chem. 36 (2001) 339–347.
[33] I.P. Kostova, I.I. Manolov, I.N. Nicolova, N.D. Danchev, Il Farmaco 56 (2001) 707–713.
[34] I. Georgieva, N. Trendafilova, A. Aquino, H. Lischka, J. Phys. Chem. A 109 (2005) 11860–11869.
[35] N. De Silva, N. Minezawa, M.S. Gordon, J. Phys. Chem. B 117 (2013) 15386–15394.
[36] A.D. Becke, J. Chem. Phys. 98 (1993) 5648–5652.
[37] C. Lee, W. Yang, R.G. Parr, Phys. Rev. B 37 (1988) 785–789.
[38] M.J. Frisch, G.W. Trucks, H.B. Schlegel, G.E. Scuseria, M.A. Robb, J.R. Cheeseman, J.A. Montgomery Jr., T. Vreven, K.N. Kudin, J.C. Burant, J.M. Millam, S.S. Iyengar, J. Tomasi, V. Barone, B. Mennucci, M. Cossi, G. Scalmani, N. Rega, G.A. Petersson, H. Nakatsuji, M. Hada, M. Ehara, K. Toyota, R. Fukuda, J. Hasegawa, M. Ishida, T. Nakajima, Y. Honda, O. Kitao, H. Nakai, M. Klene, X. Li, J.E. Knox, H.P. Hratchian, J.B. Cross, V. Bakken, C. Adamo, J. Jaramillo, R. Gomperts, R.E. Stratmann, O. Yazyev, A.J. Austin, R. Cammi, C. Pomelli, J.W. Ochterski, P.Y. Ayala, K. Morokuma, G.A. Voth, P. Salvador, J.J. Dannenberg, V.G. Zakrzewski, S. Dapprich, A.D. Daniels, M.C. Strain, O. Farkas, D.K. Malick, A.D. Rabuck, K. Raghavachari, J.B. Foresman, J.V. Ortiz, Q. Cui, A.G. Baboul, S. Clifford, J. Cioslowski, B.B. Stefanov, G. Liu, A. Liashenko, P. Piskorz, I. Komaromi, R.L. Martin, D.J. Fox, T. Keith, M.A. Al-Laham, C.Y. Peng, A. Nanayakkara, M. Challacombe, P.M.W. Gill, B. Johnson, W. Chen, M.W. Wong, C. Gonzalez, J.A. Pople, Gaussian 03, Revision C.02, Gaussian, Inc., Wallingford, CT, 2004.
[39] T. Yanai, D.P. Tew, N.C. Handy, Chem. Phys. Lett. 393 (2004) 51–57.
[40] M.J.G. Peach, T. Helgaker, P. Salek, T.W. Keal, O.B. Lutnaes, D.J. Tozer, N.C. Handy, Phys. Chem. Chem. Phys. 8 (2006) 558–562.
[41] M.J. Frisch, G.W. Trucks, H.B. Schlegel, G.E. Scuseria, M.A. Robb, J.R. Cheeseman, G. Scalmani, V. Barone, B. Mennucci, G.A. Petersson, H. Nakatsuji, M. Caricato, X. Li, H.P. Hratchian, A.F. Izmaylov, J. Bloino, G. Zheng, J.L. Sonnenberg, M. Hada, M. Ehara, K. Toyota, R. Fukuda, J. Hasegawa, M. Ishida, T. Nakajima, Y. Honda, O. Kitao, H. Nakai, T. Vreven, J.A. Montgomery Jr., J.E. Peralta, F. Ogliaro, M. Bearpark, J.J. Heyd, E. Brothers, K.N. Kudin, V.N. Staroverov, R. Kobayashi, J. Normand, K. Raghavachari, A. Rendell, J.C. Burant, S.S. Iyengar, J. Tomasi, M. Cossi, N. Rega, J.M. Millam, M. Klene, J.E. Knox, J.B. Cross, V. Bakken, C. Adamo, J. Jaramillo, R. Gomperts, R.E. Stratmann, O. Yazyev, A.J. Austin, R. Cammi, C. Pomelli, J.W. Ochterski, R.L. Martin, K. Morokuma, V.G. Zakrzewski, G.A. Voth, P. Salvador, J.J. Dannenberg, S. Dapprich, A.D. Daniels, O. Farkas, J.B. Foresman, J.V. Ortiz, J. Cioslowski, D.J. Fox, Gaussian 09, Revision C.01, Gaussian Inc., Wallingford, CT, 2009.
[42] W. Zhao, W. Bian, J. Mol. Struct. (THEOCHEM) 818 (2007) 43–49.
[43] P. Datta, A.P. Mukhopadhyay, P. Manna, E.R.T. Tiekink, P.C. Sil, C. Sinha, J. Inorg. Biochem. 105 (2011) 577–588.
[44] Y. Bai, J. Du, X. Weng, Spectrochim, Acta Mol. Biomol. Spectrosc. 126 (2014) 14–20.

[45] K. Hara, T. Sato, R. Katoh, A. Furube, Y. Ohga, A. Shinpo, S. Suga, K. Sayama, H. Sugihara, H. Arakawa, J. Phys. Chem. B 107 (2002) 597–606.
[46] X. Zhang, J. Zhang, Y. Xia, J. Photochem. Photobiol. 194 (2008) 167–172.
[47] Y. Xue, L. An, Y. Zheng, L. Zhang, X. Gong, Y. Qian, Y. Liu, Comp. Theor. Chem. 981 (2012) 90–99.
[48] M. Caricato, B. Mennucci, J. Tomasi, F. Ingrosso, R. Cammi, S. Corni, G. Scalmani, J. Chem. Phys. 124 (2006) 124520–124532.
[49] A.D. Dwyer, D.J. Tozer, Phys. Chem. Chem. Phys. 12 (2010) 2816–2818.
[50] M.R. Silva-Junior, M. Schreiber, S.P.A. Sauer, W. Thiel, J. Chem. Phys. 129 (2008) 104103–104114.
[51] D. Jacquemin, V. Wathelet, E.A. Perpète, C. Adamo, J. Chem. Theory Comput. 5 (2009) 2420–2435.
[52] L. Goerigk, S. Grimme, J. Chem. Phys. 132 (2010) 184103–184109.
[53] D. Jacquemin, J. Preat, E.A. Perpète, C. Adamo, Int. J. Quantum Chem. 110 (2010) 2121–2129.
[54] D. Jacquemin, E.A. Perpète, G.E. Scuseria, I. Ciofini, C. Adamo, J. Chem. Theory Comput. 4 (2008) 123–135.
[55] N. Yasarawan, K. Thipyapong, S. Sirichai, V. Ruangpornvisuti, J. Mol. Struct. 1047 (2013) 344–357.
[56] T.A.O. Fonseca, M.P. Freitas, R.A. Cormanich, T.C. Ramalho, C.F. Tormena, R. Rittner, Beilstein J. Org. Chem. 8 (2012) 112–117.
[57] H. Moghanian, A. Mobinikhaledi, R. Monjezi, J. Mol. Struct. 1052 (2013) 135–145.
[58] K.J. Laidler, M.C. King, J. Phys. Chem. 87 (1983) 2657–2664.
[59] A.O. Doroshenko, E.A. Posokhov, A.A. Verezubova, L.M. Ptyagina, J. Phys. Org. Chem. 13 (2000) 253–265.
[60] F.A. Villamena, J.K. Merle, C.M. Hadad, J.L. Zweier, J. Phys. Chem. A 111 (2007) 9995–10001.
[61] A. Suwattanamala, V. Ruangpornvisuti, Struct. Chem. 20 (2009) 619–631.
[62] S. Roy, T.K. Mondal, P. Mitra, E.L. Torres, C. Sinha, Polyhedron 30 (2011) 913–922.
[63] B.S. Creaven, M. Devereux, I. Georgieva, D. Karcz, M. McCann, N. Trendafilova, M. Walsh, Spectrochim, Acta Mol. Biomol. Spectrosc. 84 (2011) 275–285.
[64] I. Georgieva, T. Mihaylov, N. Trendafilova, J. Inorg. Biochem. 135 (2014) 100–112.
[65] D. Sarkar, A.K. Pramanik, T.K. Mondal, J. Lumin. 146 (2014) 480–485.
[66] O.S. Wolfbeis, Z. Phys. Chem. 125 (1981) 15–20.
[67] I. Georgieva, N. Trendafilova, A.J.A. Aquino, H. Lischka, J. Phys. Chem. A 111 (2006) 127–135.
[68] V. Barone, M. Cossi, J. Phys. Chem. A 102 (1998) 1995–2001.